Supporting Information

Kast et al. 10.1073/pnas.1001941107

SI Text

Results. ***Protein labeling and phosphorylation.*** Regulatory light chain (RLC) labeling and phosphorylation were quantitated using electrospray mass spectrometry, as exemplified for A7C/M129C in Fig. S1*A*. The peak corresponding to unlabeled RLC (U, gray) is completely eliminated by labeling (blue), producing peaks (masses) corresponding to donor-acceptor-labeled RLC (DA) and acceptor-acceptor-labeled RLC (AA). Upon phosphorylation (red), each of these peaks is shifted by 96 Da (pDA and pAA). Thus the majority of donors are on RLCs containing acceptor, and virtually all donor-acceptor-labeled RLCs become phosphorylated.

Actin-activated ATPase activity. In order to ensure that subfragment 1 (S1) samples were functionally active, actin-activated ATPase activity was measured for all samples used for fluorescence resonance energy transfer (FRET). All three mutants have comparable activities to control WT S1 (Fig. S1*B*). There was no significant difference between unphosphorylated and phosphorylated samples, as expected (2).

Time-resolved fluorescence of donor-only samples, multiexponential fits. The fluorescence of the donor-only sample, $F_{D\mathrm{obs}}(t)$ (Fig. S3*A*) was fitted by (Eq. **1**), varying the number of exponentials (n) from 1 to 4. In all cases, residuals and χ^2 values were improved by increasing n to 3, but no further improvement was observed for $n = 4$, as shown for one mutant in Fig. S3 and Table S1.

Comparison of mean distances and FWHM. Fitting datasets independently to the 2G model (Eq. **4**) yielded similar centers (R_j in Eq. **4**, Fig. S3*A*) and widths (FWHM_i in Eq. **4**, Fig. S3*B*) of the Gaussian interprobe distance distributions, for unphosphorylated and phosphorylated biochemical states (compare adjacent red and gray bars in Fig. S3). This observation justified fitting the two biochemical states globally with Eqs. **2**–**4**, assuming that both unphosphorylated and phosphorylated samples share the same closed (R_1, FWHM_1) and open (R_2, FWHM_2) structural states, with only the mol fractions differing. This procedure yielded χ^2 values that were comparable to those of independent fits, so the results of global fits are presented in Fig. 3 and in Table 1.

Fluorescence anisotropy. In principal, FRET measurements of interprobe distance can have a large uncertainty due to the unknown relative orientations of the two probes, especially if the probes are immobilized on the nanosecond timescale (3). To estimate this uncertainty, time-resolved anisotropy was measured for (5-({2-[(iodoacetyl)amino]ethyl}amino)naphthalene-1-sulfonic acid)) (IAEDANS) labeled and fluorescein-labeled RLC exchanged onto S1. All samples (5 μM S1 in a buffer containing, 150 mM NaCl, 1 mM DTT, 1 mM EGTA, 30 mM Tris · HCl, pH 7.5) were measured as described in *Methods*, except that the emission polarizer was set at 0°, 54.7°, and 90°, relative to vertical. Waveforms measured at the magic angle (54.7°, where there can be no effect of rotational motion) were fitted by Eq. **1** ($n = 3$), and the resulting lifetimes (τ_i) and amplitudes (A_i) were used to constrain these parameters in the 0° and 90° fits to

$$\begin{aligned} F(0°,t) &= (1/3)F(54.7°,t)[1 + 2r(t)], \\ F(90°,t) &= (1/3)F(54.7°,t)[1 - 2r(t)], \end{aligned} \qquad \textbf{[S1]}$$

$$r(t) = r_\infty + \sum_{i=1}^{n} r_i \exp(-t/\tau_{Ri}), \qquad r_0 = r_\infty + \sum_{i=1}^{n} r_i \qquad \textbf{[S2]}$$

The equations above were fitted globally to the 0° and 90° datasets, and the depolarization due to subnanosecond probe rotational motion was calculated as $\langle d_p^x \rangle = (r_0/r_f)^{1/2}$, where p is either D (donor) or A (acceptor). Values for r_f, the anisotropy of a rigid ensemble of probes, were assumed to be 0.4, which is an excellent approximation for both probes used here (4). These depolarizations were then used to calculate κ^2_{min} and κ^2_{max}, as described previously (3) (Table S2).

$$\langle \kappa^2 \rangle_{\mathrm{min}} = (2/3)[1 - (\langle d_D^x \rangle - \langle d_A^x \rangle)] \qquad \textbf{[S3]}$$

$$\langle \kappa^2 \rangle_{\mathrm{max}} = (2/3)(1 + \langle d_D^x \rangle^2 + \langle d_A^x \rangle^2 + 3\langle d_D^x \rangle \langle d_A^x \rangle) \qquad \textbf{[S4]}$$

R_{min} and R_{max} were calculated using Eqs. **S3** and **S4**,

$$R_{\mathrm{min/max}} = [(3/2)\langle \kappa^2 \rangle_{\mathrm{min/max}}]^{1/6} R(\kappa^2 = 2/3) \qquad \textbf{[S5]}$$

The initial anisotropy values r_0 were all quite low (Table S2), indicating nearly isotropic rotational motion on the subnanosecond timescale, thus minimizing uncertainties in the measurement of R. For each of the three mutants, uncertainty in κ^2 yields minimum and maximum distances that are ~0.9 and ~1.15 of the measured R (Eq. **S5**).

The low anisotropy values offer an additional benefit for the interpretation of FRET data. A significant source of uncertainty in FRET measurements is the long flexible linker between C_α and the fluorescent probe. However, in the present case, because we found that both donor and acceptor probes are undergoing nearly isotropic rotation on the subnanosecond timescale, much faster than the 20-ns excited-state lifetime (Fig. S2), the apparent probe location in space is effectively averaged (5), so that C_α is a good approximation for the effective location of the probe, for purposes of FRET distance measurement. Thus probe–probe distances measured by FRET should be accurate reflections of C_α–C_α distances [or slight underestimates, (5)], and the disorder measured (FWHM in Eq. **4**) should reflect only the disorder that is slower than the nanosecond timescale—which is determined primarily by the peptide backbone. Indeed, the interprobe distance distributions measured by FRET agree much better with molecular dynamics (MD) simulations calculated from C_α positions (Fig. 4*C*) than C_β or C_γ.

Distance trajectories and distributions. Interprobe distance trajectories (Fig. S4, *Left*) were used to calculate distance distributions (Fig. S4, *Right*) by allocating the C_α–C_α distances from the distance trajectories to 0.1-nm bins and normalizing to the total number of snapshots in each trajectory (3,612 for a 70-ns and 5,002 for a 100-ns trajectory). The average distribution displayed in Fig. 4*C*, shown as the thick black curve in Fig. S4 as the weighted average of the four distributions. All distributions are

bimodal, with the exception of two unphosphorylated trajectories (U2 and U4) that stay in the closed state and one phosphorylated trajectory (P1) that stays in the open state.

Root-mean-square deviation. The backbone rmsds from the initial structure are shown in Fig. S5, for the entire RLC and for its two subdomains. Root-mean-square deviation levels, as well as the amplitude of fluctuations in rmsd, are generally greater when the entire RLC is included (Fig. S5*A*) than when each domain is analyzed separately, aligned to itself (Fig. S5 *B* and *C*). This demonstrates that a major source of structural fluctuations is movement of phosphorylation domain (PD) relative to the rest of RLC (Fig. S5*A*). In most cases, rmsd values approach apparent steady states within a few nanoseconds, but these levels (and the amplitude of fluctuations in rmsd) are generally greater after phosphorylation (Fig. S5 *A* and *C*, *Right*), and during periods in which the trajectory is in the open state, which is favored by phosphorylation (Fig. 4 *B* and *C*).

Convergence. Convergence was evaluated by examining the time evolution of the cumulative mean interprobe distance over the simulated trajectories. The mean value of the 2/129 C_α–C_α distance (Fig. 4*B*) was calculated as a function of cumulative time, in either the closed or open structural states, in both the unphosphorylated and phosphorylated biochemical states (Fig. S6). These mean values showed good convergence in most cases and agreed well with experimental values (dashed lines in Fig. S6). However, due to the low frequency of transitions between open and closed states (Fig. 4*B*), the ratio of populations in open and closed states did not converge completely during our simulations.

Interdomain salt bridges in the closed state. MD simulations show that R4 plays a significant role in stabilizing the closed state of the RLC by interacting with E99 and/or D100 on the C lobe (Fig. 5 and Fig. S7). In the unphosphorylated biochemical state, at least one of these *inter*domain salt bridges is formed 72% of the time that the RLC is in the closed structural state (Fig. S7, black bars), but this number falls by a factor of 3 after phosphorylation (Fig. S7, red bars), when the closed state itself is substantially less populated, as shown by both experiment and simulation (Fig. 4*C*). This salt bridge is completely absent in the open structural state. In contrast, R16 and pS19 form an *intra*domain salt bridge in the phosphorylated PD, stabilizing the open state and thus playing a role in disrupting the interdomain salt bridges.

Methods. ***Protein preparation.*** Smooth muscle myosin and myosin light chain kinase were prepared from frozen chicken gizzards. S1 was prepared by digesting myosin with *Staphylococcus* V8 protease (2) and isolating S1 by size-exclusion chromatography. Protein concentrations were calculated using extinction coefficients of 2.69×10^5 $M^{-1}\,cm^{-1}$ (280 nm) for smooth muscle myosin and 8.17×10^4 $M^{-1}\,cm^{-1}$ (280 nm) for S1 (2). Mutant chicken gizzard RLCs were expressed in *Escherichia coli* using the Pet3a expression system (Novagen). RLCs were purified from solubilized inclusion bodies, by using a Hi-Trap anion-exchange column (6). RLC concentration was determined by using an extinction coefficient of 6740 $M^{-1}\,cm^{-1}$ (277 nm) (7).

Labeling. A solution of 50 μM RLC [20 mM 4-(2-hydroxyethyl)piperazine-1-propanesulfonic acide, pH 8.0, 50 mM NaCl, and 2 mM EDTA] was reduced with 5 mM DTT (Sigma) for 10 min. Reducing agent was removed by Zeba desalting columns (Pierce) and either 15 μM or 50 μM IAEDANS (Invitrogen) was added and incubated for 30 min at 4 °C. Excess dye was removed using successive spin columns, and extent of donor labeling was determined by two methods: (*i*) ratio of the concentration determined by UV-visible at 338 nm ($\varepsilon = 5,700$) to the protein concentration determined by Bradford (Bio-Rad), and (*ii*) electrospray (see below). Typically about 30% of available cysteines were labeled with donor. To a solution of donor-labeled RLC, 100 μM of fluorescein maleimide (Invitrogen) and 50 μM tris(2-carboxyethyl)phosphine (Invitrogen) were added. The labeling reaction was quenched with excess DTT (5 mM), and free dye was again removed using Zeba desalting columns (Pierce). The final populations of labeled RLCs were determined using electrospray mass spectrometry (Fig. S1*A*).

Thiophosphorylation. A 100-μM solution of labeled RLC was buffer-exchanged into phosphorylation buffer (25 mM Tris, pH 7.5, 50 mM NaCl, 2 mM $MgCl_2$, 2 mM $CaCl_2$) using Zeba Desalting columns (Pierce). RLC was phosphorylated by incubating with 30 μg/mL tissue purified myosin light chain kinase, 5 μg/mL Calmodulin (Pierce) and 2 mM ATPγS for 1 h at 25 °C. The reaction was stopped by adding 2 mM EGTA. Extent of phosphorylation was examined using electro spray ionization mass spectrometry (see below).

RLC exchange. Both RLC and S1 were dialyzed into exchange solution (50 mM NaCl, 5 mM EDTA, 2 mM EGTA, 1 mM DTT, 10 mM $NaPO_4$, pH 7.5). RLCs were exchanged by adding 5 mM EDTA, 2 mM ATP, and 250 μM labeled RLC (in exchange solution) to a solution containing 25 μM S1 (in exchange solution). After a 45 min incubation at 42 °C, 15 mM $MgCl_2$ was added slowly, and the exchanged S1 was immediately dialyzed into smS1 solution (50 mM NaCl, 0.2 mM EDTA, 1 mM DTT, 25 mM Tris · HCl, pH 7.5). These samples were clarified, incubated with 25 μM actin for 1 h at 25 °C, and centrifuged at $50,000 \times g$. The pellet was resuspended in smS1 solution and pelleted again. This process was repeated three more times to ensure that all excess RLCs were removed. The final wash pellet was resuspended in smS1 solution plus 10 mM ATP and 1 mM $MgCl_2$ and centrifuged. The extraction was repeated one more time and supernatants from both extractions were dialyzed extensively into smS1 solution to remove excess ATP. These samples were clarified and concentrated using 50,000 molecular weight cutoff Centricon (Millipore).

Mass spectrometry. Both unphosphorylated and phosphorylated RLCs (30 μM in 5 mM NH_4HCO_3 buffer at pH 7.9) were injected into a QSTAR 2 quadrupole-TOF mass spectrometer with an electrospray ionization source. Three injections at 2.5 min intervals, were performed for every sample. Mass spectra over the range of 500–2,000 m/z were recorded continuously during load buffer and protein infusions. The resulting spectra were analyzed using Analyst QS (Applied Biosystems) software.

Time-resolved fluorescence analysis. The fluorescence waveform of donor-acceptor labeled myosin before convolution, $F_{DA}(t)$, was analyzed by assuming that the only change in $F_D(t)$ was an increased rate of decay due to energy transfer

$$k_T = k_{Di}(R/R_{0i})^{-6}, \qquad \textbf{[S6]}$$

where R is the donor-acceptor distance, $k_{Di} = 1/\tau_{Di}$, and R_{0i} is the Förster distance

$$R_{0i} = 9,780(J\kappa^2 n^{-4} Q_{Di})^{1/6} \qquad \textbf{[S7]}$$

where J is the overlap integral between donor emission and acceptor absorption spectra, n is the refractive index of protein in aqueous solution (1.4), κ^2 is the orientation factor (set to 2/3, corresponding to random orientation), and Q_{Di} is the donor quantum yield, given by

$$Q_{Di} = \langle Q_D \rangle^* \tau_{Di} / \langle \tau \rangle, \quad \text{where } \langle \tau \rangle = \sum_{i=1}^{n} x_i \tau_{Di},$$

and the mean donor quantum yield ($\langle Q_D \rangle = 0.28 \pm 0.02$) was determined by comparison with a standard solution of 10 μM quinine sulfate in 0.05 M H_2SO_4 at $\lambda_{ex} = 347.5$ nm [$Q_S = 0.51$ (8)], according to the equation $Q_D = Q_S * (F_D(\lambda)/A_D(\lambda))/(F_S(\lambda)/A_S(\lambda))$, where $F_k(\lambda)$ is the integrated emission and $A_k(\lambda)$ is the absorbance at the excitation wavelength of donor-labeled myosin (D) or quinine sulfate (S).

1. Lanzetta PA, Alvarez LJ, Reinach PS, Candia OA (1979) An improved assay for nanomole amounts of inorganic phosphate. *Anal Biochem* 100:95–97.
2. Ikebe M, Hartshorne DJ (1985) Proteolysis of smooth muscle myosin by *Staphylococcus aureus* protease: Preparation of heavy meromyosin and subfragment 1 with intact 20000-dalton light chains. *Biochemistry* 24:2380–2387.
3. Dale RE, Eisinger J (1976) Intramolecular energy transfer and molecular conformation. *Proc Natl Acad Sci USA* 73:271–273.
4. Torgerson PM, Morales MF (1984) Application of the Dale-Eisinger analysis to proximity mapping in the contractile system. *Proc Natl Acad Sci USA* 81:3723–3727.
5. Thomas DD, Carlsen WF, Stryer L (1978) Fluorescence energy transfer in the rapid-diffusion limit. *Proc Natl Acad Sci USA* 75:5746–5750.
6. Wu X, Clack BA, Zhi G, Stull JT, Cremo CR (1999) Phosphorylation-dependent structural changes in the regulatory light chain domain of smooth muscle heavy meromyosin. *J Biol Chem* 274:0328–20335.
7. Nelson WD, Blakely SE, Nesmelov YE, Thomas DD (2005) Site-directed spin labeling reveals a conformational switch in the phosphorylation domain of smooth muscle myosin. *Proc Natl Acad Sci USA* 102:4000–4005.
8. Velapoldi RA, Tonnesen HH (2004) Corrected emission spectra and quantum yields for a series of fluorescent compounds in the visible spectral region. *J Fluoresc* 14:465–472.

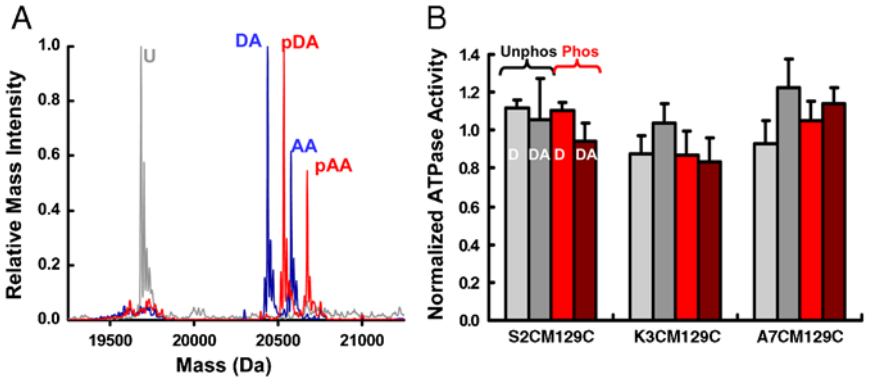

Fig. S1. (*A*) Mass spectrometry of unlabeled A7C/M129C RLC (gray) and doubly labeled A7C/M129C RLC before (blue) and after (red) phosphorylation. Peak assignments are based on the masses of donor (307.35 Da), acceptor (426.36 Da), and phosphate (96 Da). (*B*) Actin-activated ATPase activity of FRET samples. Unphosphorylated and phosphorylated donors (light gray and red) and FRET (dark gray and dark red) samples were buffer-exchanged into 50 mM NaCl, 1 mM $MgCl_2$, 0.2 mM EGTA, 30 mM Tris (pH 7.5). The reaction was started by adding 1 mM ATP to a solution containing 0.1 μM S1 and 50 μM actin. Phosphate release was measured using a malachite green molybdate assay (1). Activity of S1 was negligible in the absence of actin. Activities were normalized to that of control S1, which went through the exchange process with unlabeled RLC. Error bars are SEM ($n = 3$).

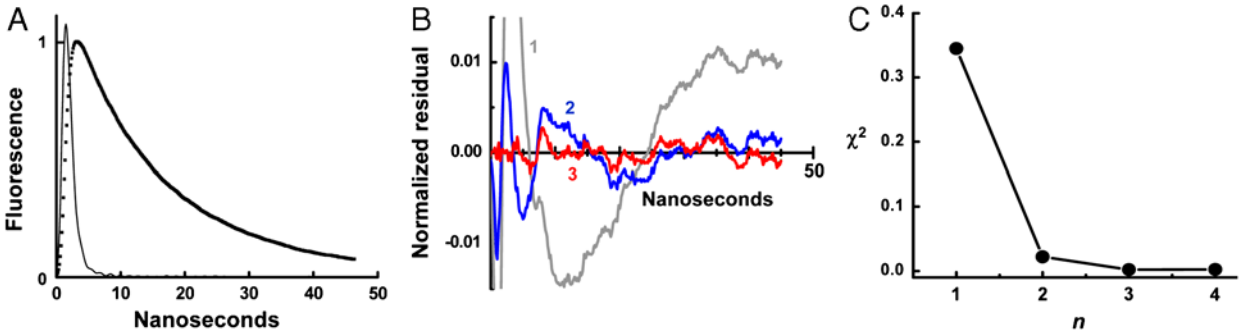

Fig. S2. Time-resolved (TR) fluorescence fit of donor-only S2C/M129C. (*A*) Fluorescence data and instrument response function. (*B*) Normalized residuals, (data – fit)/(maximum fit value), for fits with Eq. **1** for $n = 1$–3. (*C*) Reduced χ^2 values.

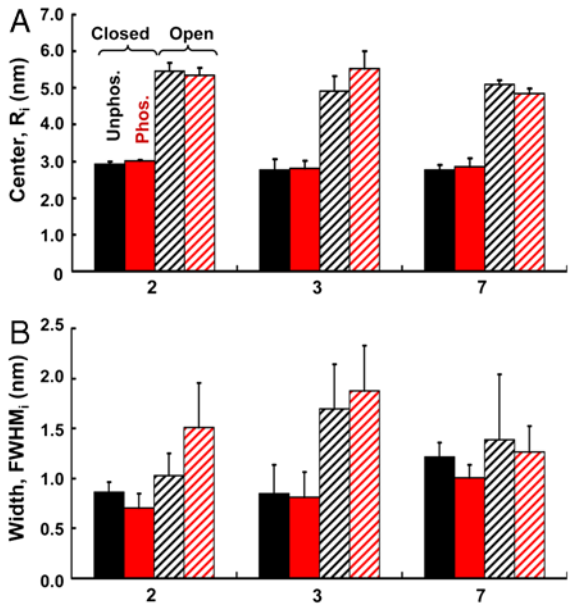

Fig. S3. Results of independent fits (Eqs. **3–5**, $n = 2$) for unphosphorylated (black) and phosphorylated (red) RLC, assuming two Gaussian distributions: closed state (solid) and open state (striped). Error bars are SEM ($n = 3$).

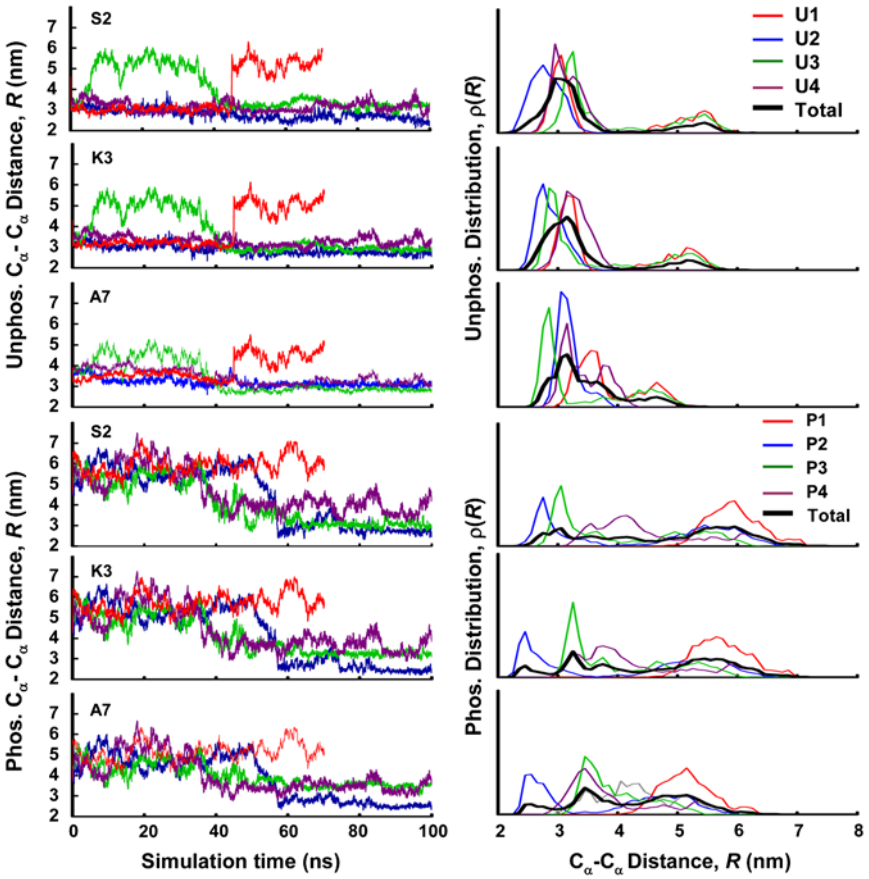

Fig. S4. RLC distance trajectories (*Left*) and distributions (*Right*). Distance trajectories $R(t)$ (*Left*) for one 70 (red) and three 100 ns (blue, green, and purple) simulations, where R is the distance between C_α of M129 to C_α of the indicated residue. These distances were used to construct the distance distributions (*Right*), using bins of 0.1-nm width.

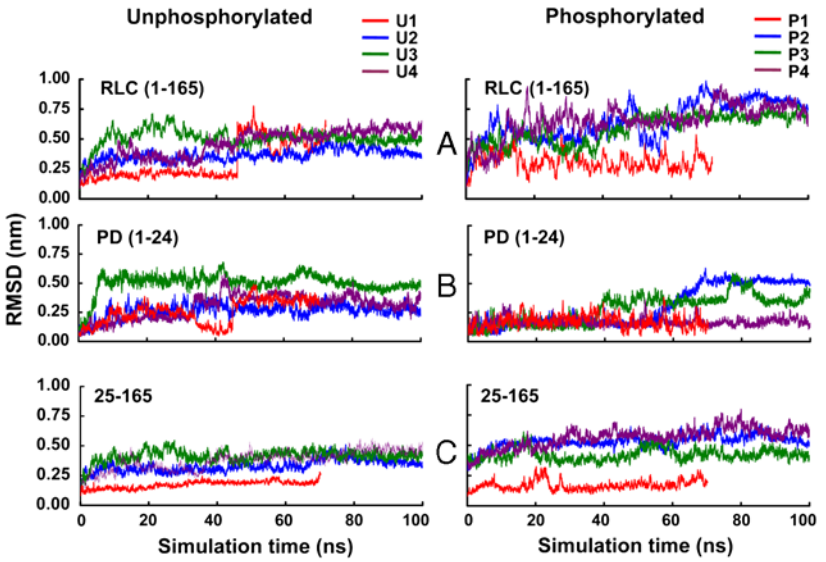

Fig. S5. Root-mean-square deviation, calculated for backbone atoms (*C*, C_α, *N*), of (*A*) the entire RLC (residues 1–165), (*B*) the PD (residues 1–24), and (*C*) the rest of the RLC (residues 25–165). Each of the three structures was aligned to itself; ie., at each time point, the new structure was aligned (rotated as a rigid body until rmsd was minimized) to the initial structure, and rmsd was calculated with respect to the initial structure.

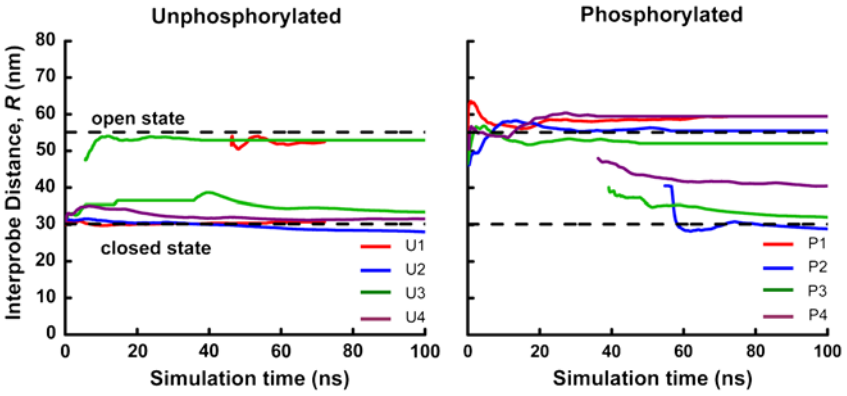

Fig. S6. Convergence to the mean for unphosphorylated (*Left*) and phosphorylated (*Right*) trajectories for the interprobe distance 2/129. The closed and open states were defined for *R* in the range of 1.5–4.5 nm, and 4.5–7.5 nm, respectively. In the unphosphorylated biochemical state (*Left*), the open and closed structural states show rapid convergence to their respective means, and more importantly, these means are similar to the means determined by TR-FRET (black dashed lines). In the phosphorylated biochemical state (*Right*), the open state (*Top*) also shows rapid convergence to values that are close to the experimental mean. The lack of rapid convergence of the closed state of phosphorylated RLC suggests (*i*) insufficient simulation time, and/or (*ii*) this state is unstable.

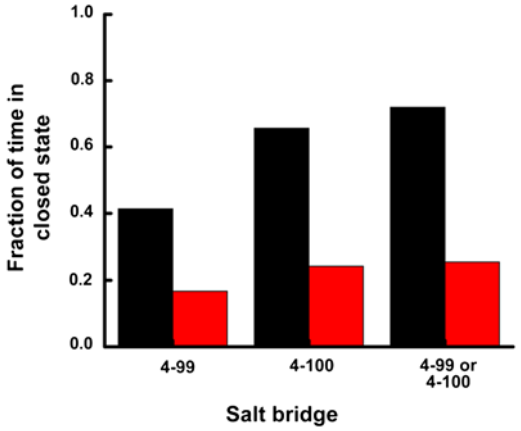

Fig. S7. Fraction of time 4–99 and 4–100 salt bridges are found during the closed structural state of unphosphorylated (black) and phosphorylated (red) RLC simulations. The hydrogen bond component of the salt bridges was calculated with visual molecular dynamics assuming a maximum proton donor-acceptor distance of 0.36 nm and a cutoff angle of 30°.

Table S1. Values for the fits in Fig. S3

	Number of lifetimes			
	1	2	3	4
x_1*	1.000	0.196	0.561	0.533
τ_1†	15.09	16.42	17.35	18.67
x_2				0.292
τ_2				13.33
x_3		0.803	0.160	0.166
τ_3		3.16	6.42	5.70
x_4			0.280	0.387
τ_4			0.51	0.51
χ^2_{reduced}	0.3450	0.0219	0.0021	0.0022

*x_i = mol fraction = normalized amplitude $A_i/(\sum_{i=1}^{n} A_i)$ (Eq. **1**).
†τ_i = fluorescence lifetime (Eq. **1**).

Table S2. Range of κ^2, based on time-resolved anisotropy (Eqs. S3 and S4)

	Initial anisotropy, r_0			
	IAEDANS	Fluorescein	κ^2_{min}*	κ^2_{max}*
S2C	0.11	−0.01	0.38	1.44
K3C	0.11	−0.03	0.36	1.48
A7C	0.13	−0.04	0.35	1.53
M129C	0.17	−0.06		

*Calculated from Eqs. **S3** and **S4**, with one probe bound to the given Cys and the other probe bound to M129C.